ADVANCED MATERIALS TECHNOLOGIES
www.advmattechnol.de

Multimaterial Microrobots for pH Sensing Fabricated Using Sequential 3D and 4D Printing with Automated Alignment

*Daniel Maher, Marcin Piekarczyk, Stefan Sützl, Andreu Murillo Vilella, Marc Fiechter, Yekaterina Tskhe, Colm Delaney, Rafael Taboryski, Larisa Florea, and Ada-Ioana Bunea**

Microscale pH sensing is important for the study and control of biological and chemical processes. While current tools for microscale pH measurements have their limitations, microrobots are a promising alternative. In this work, the use of multimaterial microrobots for microscale pH sensing is proposed. The microrobots consist of a hard polymer backbone, enabling transportation using optical trapping, and 4D printed smart material sensing elements. A custom automated alignment program is employed to ensure rapid and accurate alignment of the smart material onto the hard polymer backbone. The potential of the microrobots for pH sensing is demonstrated with visual readout from optical microscopy images. The hydrogel sensing elements exhibit a 32 ± 11% size increase from pH 2.3 to 8.8, most of which occurs between ≈pH 5 and ≈pH 7. The swelling performance shows no significant change after repeated cycling from acidic to neutral pH and storage for up to 2 months. When assessing the mobility of the microrobots, speeds of ≈14 µm s^{-1} can be reached using optical trapping in a phosphate-buffered saline solution. The swelling response, reusability, and high mobility of the microrobots make them promising tools for pH sensing in microfluidic devices.

1. Introduction

The concentration of hydrogen ions, also called protons, is critical for many biological and chemical processes. In practice, the concentration of hydrogen ions is typically expressed as a value on the pH scale, which was first introduced by S.P.L. Sørensen at Carlsberg laboratory in 1909.[1] For example, pH is used to understand cellular metabolic pathways and enzymatic reactions, particularly during drug screening tests.[2,3] pH gradients around tumor cells are also studied to understand cancer growth and how tumors metastasize.[4,5] Additionally, pH control in media is important for, e.g., optimizing the production of therapeutic proteins from cells,[6,7] culturing bacteria,[8–10] or for controlling the size of nanoparticles obtained from synthesis reactions.[11–13] This makes pH sensing an important aspect for both studying and controlling biological and chemical processes.

While measuring pH on the macroscale is rather straightforward, microscale measurements are more complicated. Currently, there are several techniques for microscale pH measurements, which all have characteristic limitations. The most widespread method involves the use of fluorescent probes, which are most often attached to nanoparticles,[14,15] or embedded inside a material.[16] Although this method allows for high precision and spatial resolution, fluorescence probes typically lose their ability to fluoresce over time due to photobleaching.[17] Scanning electrochemical microscopy[18–20] and scanning ion conductance microscopy[21,22] require an open setup and therefore cannot be used for investigations in microfluidic channels. Surface-enhanced Raman scattering requires nanopatterned surfaces or nanoparticles in the liquid media to obtain a high signal-to-noise ratio.[23,24] Ion sensitive field effect transistors have poor spatial resolution.[25–27] Consequently, alternative solutions for localized pH measurements are interesting to develop.

Microrobots are excellent candidates for use for microscale pH sensing. Over the past two decades, microrobots have seen a considerable increase in popularity[28] because they can accomplish difficult tasks on the microscale. Sensing is one of the applications microrobots are suitable for. Their small size, coupled with

D. Maher, M. Piekarczyk, S. Sützl[+], A. M. Vilella[++], M. Fiechter[+++], R. Taboryski, A.-I. Bunea
National Centre for Nano Fabrication and Characterization (DTU Nanolab)
Technical University of Denmark
Ørsted Plads 347, Kongens Lyngby 2800, Denmark
E-mail: adabu@dtu.dk

Y. Tskhe, C. Delaney, L. Florea
School of Chemistry & AMBER
Trinity College Dublin
Pearse St., Dublin 2 D02 CP49, Ireland

The ORCID identification number(s) for the author(s) of this article can be found under https://doi.org/10.1002/admt.202501075

[+]Present address: Department of Chemistry, Center for Analysis and Synthesis (CAS), Lund University, Naturvetarvägen 14, Box 124, 221 00 Lund, Sweden

[++]Present address: CERN, 1211 Geneva 23, Switzerland

[+++]Present address: Ambu A/S, Baltorpbakken 13, 2750 Ballerup, Denmark

DOI: 10.1002/admt.202501075

their maneuverability in confined spaces, makes them good candidates for localized chemical detection.[29–31]

Microscale 3D printing technologies, particularly two-photon polymerization (2PP), have simplified the process of fabricating microrobots.[32] 2PP micro printing involves scanning a tightly focused pulsed laser within the volume of a negative photoresist. The exposed areas become solid, and freeform microstructures can be fabricated.[33,34] The high resolution and versatility of 2PP have made it one of the key technologies for microrobot fabrication.[35–37]

In terms of external control, magnetic and optical manipulation are the most popular methods for 3D printed microrobots.[38,39] Both magnetic and optical manipulation have characteristic advantages and disadvantages. Magnetic manipulation is advantageous for simultaneously manipulating swarms of microrobots through various types of media, but often requires post-fabrication treatment for the magnetic properties. Optical manipulation is excellent for precisely controlling microrobots in 3D space, but requires optically transparent media. Therefore, the most suitable manipulation method depends on the application.

Various photoresists can be printed using 2PP. This includes smart materials, which are materials that change their properties in response to external stimuli such as light, chemical cues, or temperature.[40] Smart materials that can be printed using 2PP are polymer-based materials and include hydrogels, liquid crystal elastomers, shape memory polymers, and composites.[40] When subjected to a certain stimulus, the behavior of smart materials is typically a shape change. This shape response can be engineered to provide functionality, making smart materials interesting for advanced microscale applications.

The 3D printing of smart materials is known as 4D printing. The fourth dimension is time, referring to the fact that 4D printed smart materials exhibit shape changes over time. The integration of smart materials with microrobots via 4D printing has enabled the fabrication of microrobots with new and/or advanced capabilities. Already, microrobots with 4D printed components have been used for applications within, e.g., drug delivery,[41–43] micromanipulation,[44–46] or assisted reproduction.[47]

Hydrogels can swell and shrink by changing their level of hydration in a reversible manner. In the case of ionic hydrogels, the level of hydration is influenced by pH. For a more detailed discussion on the mechanisms behind this behavior, as well as examples of hydrogels responding to pH and other chemical cues, we refer interested readers to a recent review paper.[40] pH-responsive hydrogels are well-established for macroscale pH sensing.[48] However, there are only a few reports of microscale pH sensing using pH-responsive hydrogels, which primarily employ optical pH sensing methods.[49] These require specialized setups for recording and analyzing frequency shifts, which occur due to hydrogel swelling and can be correlated with the local pH. For example, Saetchnikov et al. used a pH-responsive hydrogel to 4D print optical microresonators able to detect pH changes with a detection limit of 0.003 pH units.[50] However, the microresonators reported in this work must be anchored to a substrate, and their performance is limited when subjected to pH changes larger than 1 pH unit. Another type of optical detection method employs pH-responsive hydrogels containing nanoparticles, also known as photonic crystal hydrogels, for localized pH measurements.[51–53] As the hydrogel changes shape, the spacing between the nanoparticles changes, which in turn shifts the photonic band gap generated by the periodic nanoparticles. This results in different observable structural colors, which can correlated with the local pH. However, the dispersion of nanoparticles must be periodic to obtain uniform structural colors, which makes the photonic crystal hydrogels challenging to implement.

In this work, we propose the use of mobile multimaterial microrobots for localized pH sensing. The microrobots are composed of a 3D printed hard polymer backbone, which allows for remote optical manipulation, and 4D printed pH-responsive hydrogel features, which act as the sensing elements. The pH-responsive hydrogel we used is an anionic hydrogel, which means that the material swells with increasing pH. The pH sensing method we propose is based on size quantification of the sensing elements, which can be done from optical microscopy images. The multimaterial microrobots are fabricated by 2PP in a two-step printing process, which requires alignment between the two steps. To streamline the fabrication process, we developed an automated alignment program based on computer vision. The automated alignment program is employed to ensure fast and precise alignment of the hydrogel sensing elements onto the microrobot backbones during fabrication.

The microrobot sensing elements show a sigmoid response to pH changes, with an area increase of 32 ± 11% from pH 2.3 to pH 8.8 and a linear range from ≈pH 5 to ≈pH 7. The microrobot swelling performance showed no signs of degradation after cycling from acidic to neutral pH, even after 8 weeks of repeated testing. Optical trapping is used to maneuver the microrobots in liquids, enabling precise positioning in 3D space.[54] The microrobot can be manipulated with speeds up to ≈14 μm s^{-1} in a solution consisting of phosphate-buffered saline (PBS) with surfactant. Thus, the microrobot can be transported to target locations, where the local pH can be estimated by measuring the size of the sensing elements. The mobility and pH response of our microrobots make them promising tools for localized pH sensing applications.

2. Results and Discussion

2.1. Microrobot Design

When designing our microrobots, we took into account several factors related to both maneuverability and pH sensing. We conceptualized several different designs and tested them in an iterative process (data not shown). **Figure 1** shows the final microrobot design and representative microscopy images of the fabricated microrobots.

For maneuverability, we considered the overall size of the microrobots, the number of trapping handles, and the material for the trapping handles. For optical trapping, the microrobots must be small enough to fit within the 70 μm diameter trapping area of our optical trapping setup. To enable movement with six degrees of freedom, the microrobots should have at least three spherical trapping handles. The trapping handles should be an order of magnitude larger than the wavelength used, enabling optical trapping in the Mie regime.[54] To keep the overall microrobot size low while fulfilling the trapping handles requirements, we chose to include three spheres with a diameter of 10 μm each. The

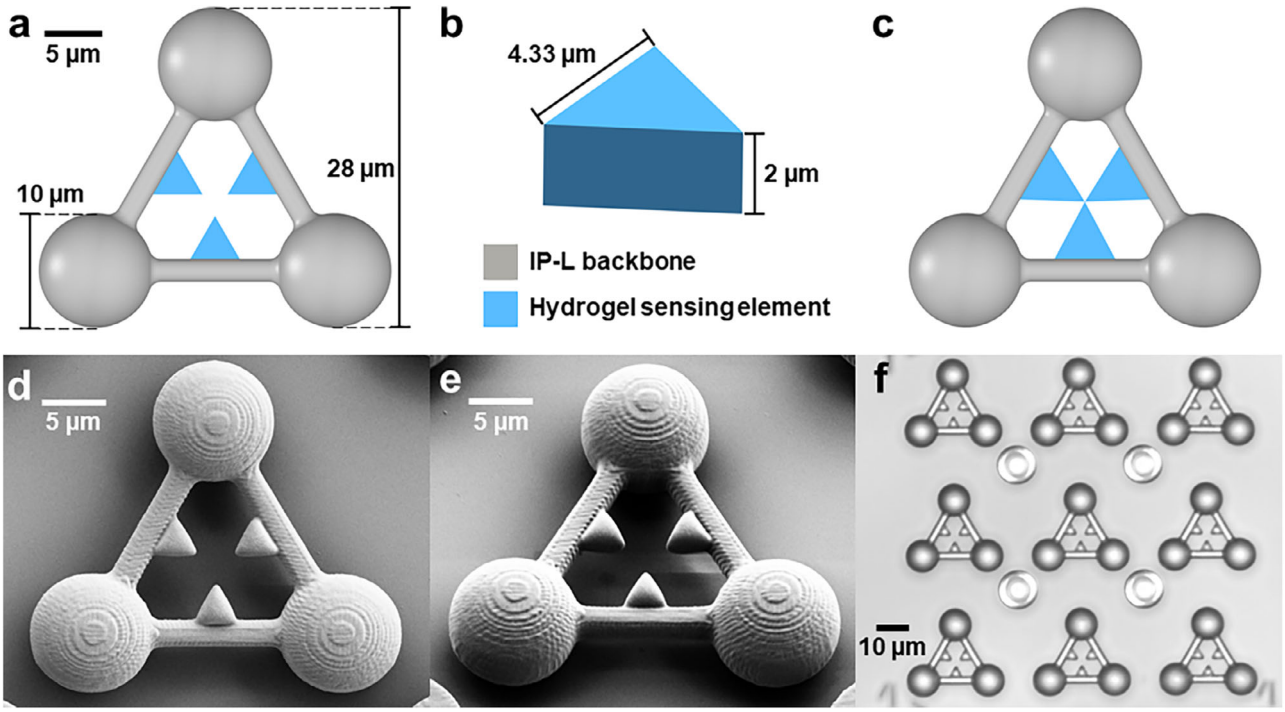

Figure 1. Multimaterial microrobot design and microscopy images. a) Microrobot design consisting of a hard polymer backbone (gray) and a pH-responsive hydrogel (blue). b) Isometric view of the sensing element, which is an equilateral triangular prism. c) Microrobot in the "on" state: the three sensing elements swell and come into contact when the pH is >7. d,e) Scanning electron micrographs of a microrobot at d) 0° (top view) and e) 30° tilt angle. f) Optical microscope image of fabricated microrobots in air.

overall dimensions of the microrobots are similar to previous microrobots fabricated in our lab.[55] For optical trapping, the material of the microrobot should also have a good refractive index contrast against water, and hydrogel materials do not fit this requirement. Thus, we chose to include a hard polymer backbone in our microrobots. The hard polymer chosen has a refractive index of ≈1.5 at a wavelength of 1 µm, which makes it suitable for optical trapping.[56] This resulted in a multimaterial microrobot design in which the hard polymer backbone is used for optical trapping, while the sensing elements are made of a pH-responsive hydrogel smart material 4D printed onto the backbone (Figure 1a).

For sensing, we wanted to include sensing elements suitable for both qualitative and quantitative visual estimation of pH. An anionic pH-responsive hydrogel, which swells with increasing pH, was chosen for the sensing element. We conducted preliminary experiments (data not shown) for the shape and size of the sensing elements. We decided to use an equilateral triangular prism shape (Figure 1b), which exhibited good structural stability during printing. The size of the sensing element was selected as a compromise between the swelling behavior, where smaller structures exhibit higher swelling, and quantification criteria, where a larger structure is easier to visualize and measure. To allow for a rough qualitative estimation of the pH, we arranged the prisms onto the backbone in such a way that they should touch when the pH is above 7 (Figure 1c). The size of the sensing elements was designed to enable this behavior. For this purpose, we used experimental swelling results to select the target size of the sensing elements for the fabrication process. More specifically, we adjusted the size of the sensing elements such that they would only touch in the case of maximum swelling, i.e., average swelling + standard deviation. In this way, we ensure that there is no overlap between the sensing elements in neutral pH, which could limit further swelling and thus reduce the sensing accuracy. Additionally, the sensing elements can be used for quantitative pH measurements, which require calculating the top area of the hydrogel prisms in different conditions. Having three sensing elements on each microrobot allows for triplicate measurements with a single microrobot.

2.2. Microrobot Fabrication

We performed a study to select the optimal print parameters for the pH-responsive hydrogel photoresist sensing elements before fabricating the multimaterial microrobots. We varied the laser power (35–55 mW), scan speed (5–10 mm s^{-1}), slicing distance (0.2–0.4 µm), hatching distance (0.2–0.3 µm), print orientation (0°, 90°, or woodpile), and number of contour lines (0 or 1). We observed that these parameters affect both the printing of the sensing elements and their response. In terms of printing, certain parameter combinations resulted in more robust structures, while others resulted in structures more prone to bending or even collapsing. Different parameter combinations also resulted in large differences in the actuation response of the sensing elements, with a degree of swelling ranging from ≈10% to ≈50%. Increasing the exposure dose withing the sensing elements can be done by increasing the laser power, or by decreasing the

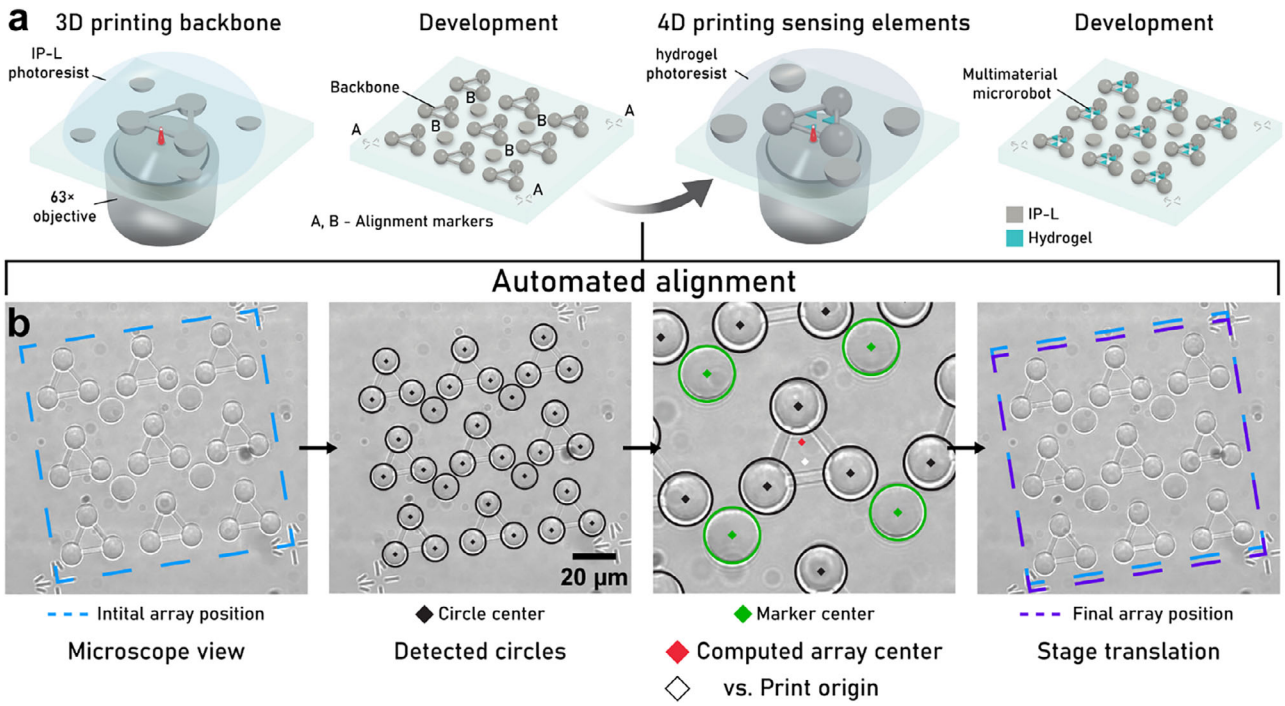

Figure 2. Process flow for fabricating multimaterial microrobots using 2PP. a) Fabrication steps using 2PP on a Nanoscribe Photonic Professional GT+ system. The microrobot backbones are printed with alignment markers to assist with the 4D printing of the sensing elements. b) Automated alignment program flow. A circle Hough transform is used to identify circles (black) in the image. The array center (red) is computed using the positions of the four alignment markers (green). The program moves the stage such that the center of the backbone array and the print origin (white) are aligned.

scan speed, slicing distance, or hatching distance. As expected, a higher exposure dose gives better structural integrity, which can be attributed to a higher degree of conversion inside the material, as well as higher values of the Young's modulus.[57,58] However, structures fabricated with the highest exposure doses showed a lower degree of swelling, ≈10% from pH 2.3 to 8.8 (data not shown). The structures fabricated with the lowest exposure doses showed a higher degree of swelling, up to ≈50%, but they showed lower reproducibility and were prone to mechanical failure. Since a larger response is preferable for the sensing application, but structural integrity is also important, we selected intermediary parameters, which gave a good compromise between the two (see section "Microrobot Fabrication").

Figure 2 shows the process flow for fabricating the multimaterial microrobots, which involves two sequential printing steps and an automated alignment process (Figure 2a). In the first printing step, we use a hard polymer material to print the hard polymer backbones and two types of alignment markers. Nine backbones, arranged in a 3 × 3 array, are printed in ≈1 min. The rotation alignment markers (A) are arrow-like symbols printed in the corners of the microrobot backbone array. These rotation alignment markers are used to manually rotate the print coordinate system after the first development step. The automated alignment markers (B) are four hemispheres printed inside each microrobot backbone array. These automated alignment markers are used by the automated alignment program to reposition the stage for printing the sensing elements onto the backbones.

The alignment program we developed (Figure 2b) uses the circle Hough transform to detect all circles in the microscope view, followed by an algorithm that identifies the four automated alignment markers (manuscript in preparation). Once the automated alignment markers are identified, their positions are used to calculate the center of the backbone array. The program then instructs the stage to move in order to align the print job origin on the computed array center, which effectively results in aligning the sensing elements onto the backbones. The process is repeated iteratively maximum five times until the misalignment between the center of the array and the print origin (i.e., where (X,Y) = (0,0) is on the print coordinate system) is less than 0.2 µm. The automated alignment program takes 5–10 s per microrobot array. Printing the sensing elements for one microrobot backbone array then takes another ≈5 s.

Figure 1d,e show representative scanning electron microscopy (SEM) images of a printed microrobot, from which it is apparent that the sensing elements are positioned correctly. Figure 1f shows an optical microscope image of an array of microrobots after development. From SEM images, we calculated the misalignment of the sensing elements onto the backbones, which is ± 0.35 µm (Figure S1 and Table S1, Supporting Information). This is better than the stage repeatability of <1.5 µm reported by the supplier for our 2PP system. Thus, our automated alignment program allows us to streamline multimaterial fabrication with high alignment accuracy.

The use of automated alignment has several advantages. Its use minimizes alignment errors that may arise from user choices when performing the alignment manually. The alignment process is more reproducible, while the workload of the 2PP operator is reduced, compared to manual alignment. The program

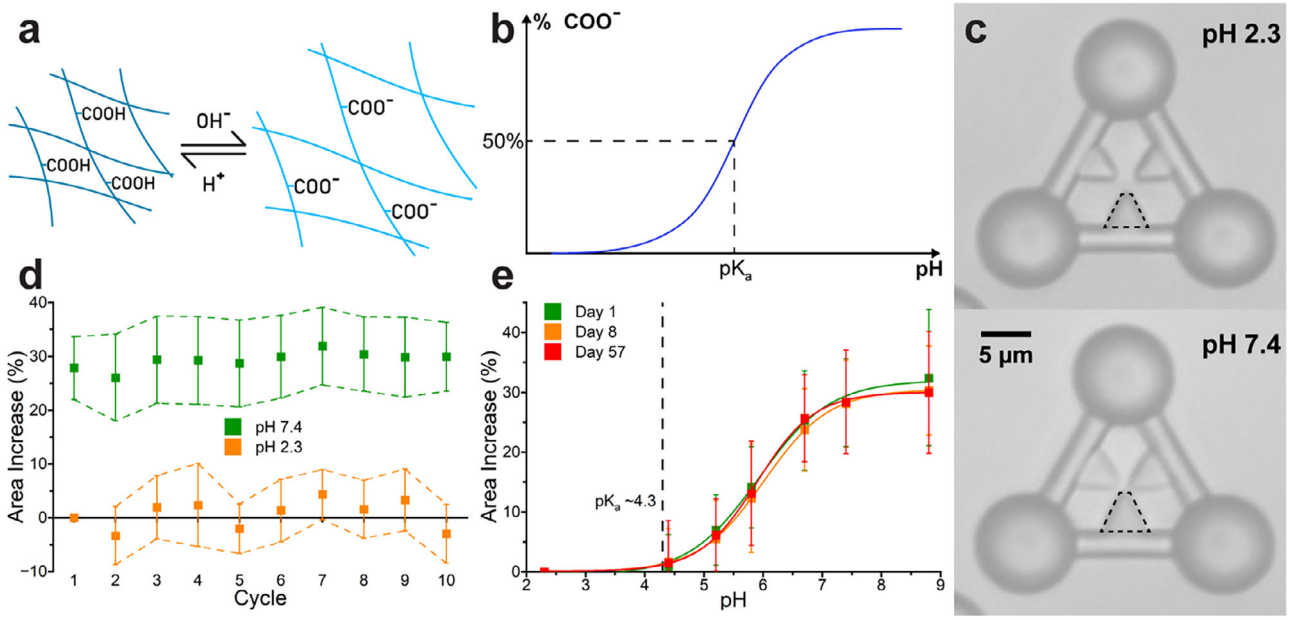

Figure 3. Characterization of the swelling behavior of the pH-responsive hydrogel. a) Schematic drawing of the pH-responsive hydrogel network reversible swelling mechanism. b) Relationship between percentage of deprotonated carboxyl groups and the pH for a pH-responsive hydrogel. ≈50% of the carboxyl groups are deprotonated when the pH is equal to the pK_a of the hydrogel. c) Optical microscope images of the microrobot in pH 2.3 and 7.4 solutions. The dashed lines show an example for how the sensing element area is defined for measurements. d) pH cycling from pH 2.3 to 7.4, which shows the short-term stability of the sensing elements' swelling response ($n = 27$). e) Area % increase of the sensing elements as a function of pH ($n = 27$). The same microrobots were investigated at different time points over a period of 2 months. The results obtained after 1, 8, and 57 days are shown in the graph. The data points are fitted using Boltzmann sigmoid fits.

corrects for intrinsic stage movement errors when printing multiple arrays by performing the alignment for each individual array. Finally, the automated alignment program is relatively fast, reducing the total fabrication time. For the microrobot design shown in this paper, the printing throughput is of ≈450 microrobots per hour, excluding development and drying times.

2.3. Sensing Behavior

Our sensing method relies on visually observing and quantifying the shape change of the pH-responsive hydrogel sensing elements from optical microscopy images. To assess the microrobots' potential for pH sensing, we investigated the swelling hydrogel sensing elements as a function of pH. For this purpose, we added liquids with various pH values to the substrates containing the printed structures, and we imaged the microrobots while immersed in the liquids. The microscopy images were acquired at least 5 s after adding the liquid media. From our experiments, we could see that within these 5 s, the microrobots' sensing elements already reach steady-state swelling, as no further size increase is measured from images taken at a later time. The response time in order of a few seconds is in line with previous literature reports.[52,59]

Figure 3 shows the swelling behavior of our sensing elements. The pH-responsive hydrogel contains acrylic acid as the monomer. When the hydrogel photoresist is polymerized, the resulting polymer network contains carboxyl groups (—COOH) from the acrylic acid monomer. In acidic environment, these carboxyl groups are protonated (Figure 3a). The degree of protonation depends on the local pH in relation to the acid dissociation constant (pK_a) of the hydrogel. When the pH is equal to the pK_a of the hydrogel, half of the carboxyl groups in the hydrogel are protonated (—COOH) and the other half are deprotonated ($—COO^-$) (Figure 3b).[60] At pH higher than the pK_a, more carboxyl groups deprotonate, which leads to a negative charge in the hydrogel network. The repulsive electrostatic forces generated by the negatively charged $—COO^-$ groups lead to a migration of co-ions and counter-ions into the network.[61] This increases the osmotic pressure and makes the hydrogel network swell in an isotropic manner. This shape response is reversible, meaning that the hydrogel network shrinks isotropically when the pH is decreased. We examined the reversibility of the sensing elements' shape response. We repeatedly cycled between pH 2.3 and 7.4 and measured the area % change of the sensing elements (Figure 3c). As shown in Figure 3d, the sensing elements showed no sign of degradation in their swelling performance after ten cycles. We repeated this experiment on the same microrobots after 7 weeks of storage with similar results (Table S2, Supporting Information). This demonstrates the potential of our microrobots for pH sensing over several months, without loss of functionality.

We investigated the sensing elements' swelling as a function of pH (Figure 3e). We used solutions with pH up to 12.2 in preliminary experiments (data not shown). However, we decided not to use solutions with pH values above 8.8 for this study, because the measured area increase was not significant at higher pH. In addition, alkaline solutions etch the borosilicate glass substrate the microrobots are printed on, leading to their

detachment. We plotted the area % increase as a function of pH and performed a Boltzmann sigmoid fit, which shows a strong correlation (R^2 values higher than 0.99). The sensing elements begin to swell around pH 4, which is close to our hydrogel's pK_a. This is consistent with literature reports on the behavior of pH-responsive hydrogels.[62–64] The rate of swelling is highest in relation to pH changes between ≈pH 5 and ≈pH 7. At higher pH, the rate of swelling declines and a plateau is reached. In practice, this swelling behavior is not sufficient to qualify the microrobots as true pH "sensors", both because of their limited response range, and because of the relatively low signal-to-noise ratio, i.e., 32 ± 11% size increase from pH 2.3 to 8.8. Instead, our microrobots are more similar to the litmus paper commonly used on the macroscale, as they are only semi-quantitative and most suitable in the pH range of 3–8.

We further examined the effect of storage on the sensing elements' swelling response. For this purpose, the same microrobots were investigated at different time points over a period of two months. The characteristic sigmoid curve was still observed after ≈8 weeks of storage, while no noticeable degradation was seen in the swelling behavior (Figure 3e). This is an important feature for sensing, because it means the sensing could be calibrated and stored until it is needed.

Temperature can influence the ionization of hydrogels, and even the pK_a of a material is temperature-dependent. All experiments for characterizing the swelling of the sensing elements were performed in a cleanroom environment with temperature control between 21.5 and 23.5 °C and humidity control between 45% and 55% RH. All solutions used for testing were allowed to reach room temperature inside the cleanroom before use. Thus, the influence of temperature on the results obtained is most likely negligible. However, a more strict temperature control could help improve repeatability.

2.4. Microrobot Manipulation Using Optical Trapping

Microrobot maneuverability testing (**Figure 4**) was performed inside a microfluidic flow cell filled with PBS and surfactant (Figure 4a) using our optical trapping setup, which uses counter-propagating beams (Figure S2, Supporting Information).[55] Figure 4b shows side view snapshots of the microrobot being translated vertically in the flow cell. We were able to translate the microrobots upward, against gravity, with a speed of ≈7 µm s^{-1}. Figure 4c shows top view snapshots of the microrobot being translated within the trapping area (large white circle). Likewise, Figure 4d shows top view snapshots of the microrobot being rotated within the trapping area. The microrobot responds well to the optical traps and can be translated in XY at ≈14 µm s^{-1} and rotated at ≈80° s^{-1} within the trapping area. Moving the traps at a faster speed makes the microrobot unable to follow the traps, which means that it remains stationary. To transport the microrobot to different regions of the flow cell, the sample stage can be translated while keeping the optical traps stationary (Video S1, Supporting Information). In this way, the microrobot is held in place with the optical traps, while the sample itself is moving. The maximum speed the sample stage could be moved while having the microrobot held by the traps is ≈26 µm s^{-1}. This shows that the microrobot can be repositioned to different regions of a sample to measure pH in those areas. To confirm microrobot mobility in different pH environments, we repeated the same optical trapping experiments with the microrobots immersed in a pH 2.3 solution. The microrobots responded well to the traps and similar movement speeds were observed (Video S2, Supporting Information). This confirms that our microrobots can be controlled in 3D space in environments with different pH.

One limitation of our optical trapping setup, which uses two sets of counter-propagating beams to control the microrobot, is that it is difficult to observe the sensing element while the bottom objective is in focus. This means that it is only possible to clearly observe the sensing element while the bottom objective is unfocused, in which case the microrobot trapping is less effective. Figure 4e shows top-view images of the microrobot in pH 2.3 and 7.4 acquired while the bottom objective is unfocused. The sensing element can be clearly observed in this case. Furthermore, it can be seen that the microrobot is in the "on" state in the bottom picture, i.e., that the sensing elements are touching. Hence, we confirm that the microrobot can be positioned in an area, imaged, and then transported by optical trapping to another location.

3. Conclusion

We designed and fabricated multimaterial microrobots for pH sensing. We characterized the microrobots' pH response. The hydrogel sensing elements exhibited a 32 ± 11% size increase from pH 2.3 to 8.8. Based on this swelling, the developed microrobots allow for qualitative visual assessment of whether the local environment is acidic or basic, as the microrobot sensing elements touch at pH >7. Furthermore, the microrobots could be suitable for quantitative pH sensing in the pH range of ≈5 to ≈7, where they exhibit the highest response to pH changes. The pH response showed good repeatability over ten cycles and no significant changes even after 8 weeks of storage, which means the microrobots can be stored and reused as needed. The fabricated microrobots were deployed in flow cells, where they could be transported using optical trapping with good maneuverability. The microrobots could be manipulated in 3D, where they could be, e.g., translated in XY at ≈14 µm s^{-1} and rotated at ≈80° s^{-1} in a PBS solution.

To streamline the fabrication of our multimaterial microrobots, we employed a custom automated alignment program, which enables the fabrication of multimaterial structures with a misalignment of ±0.35 µm. To the best of our knowledge, this is the first use of automated alignment for multimaterial microrobot fabrication using 2PP. The use of automated alignment reduces the need for manual user input, which in turn reduces the workload of the user, and enables good repeatability and rapid fabrication of multimaterial microstructures.

The swelling response, reusability, and high mobility of our microrobots make them promising tools for pH sensing in microfluidic devices. Compared to other established methods for microscale pH sensing, our approach is suitable for use in microfluidic channels, does not require the addition or removal of chemicals from the sensing environment, and shows good stability over time, even with repeated use. Compared to previous reports of using hydrogels for microscale pH sensing, our approach is significantly easier to implement, since it only requires optical microscopy images. This makes it possible to integrate

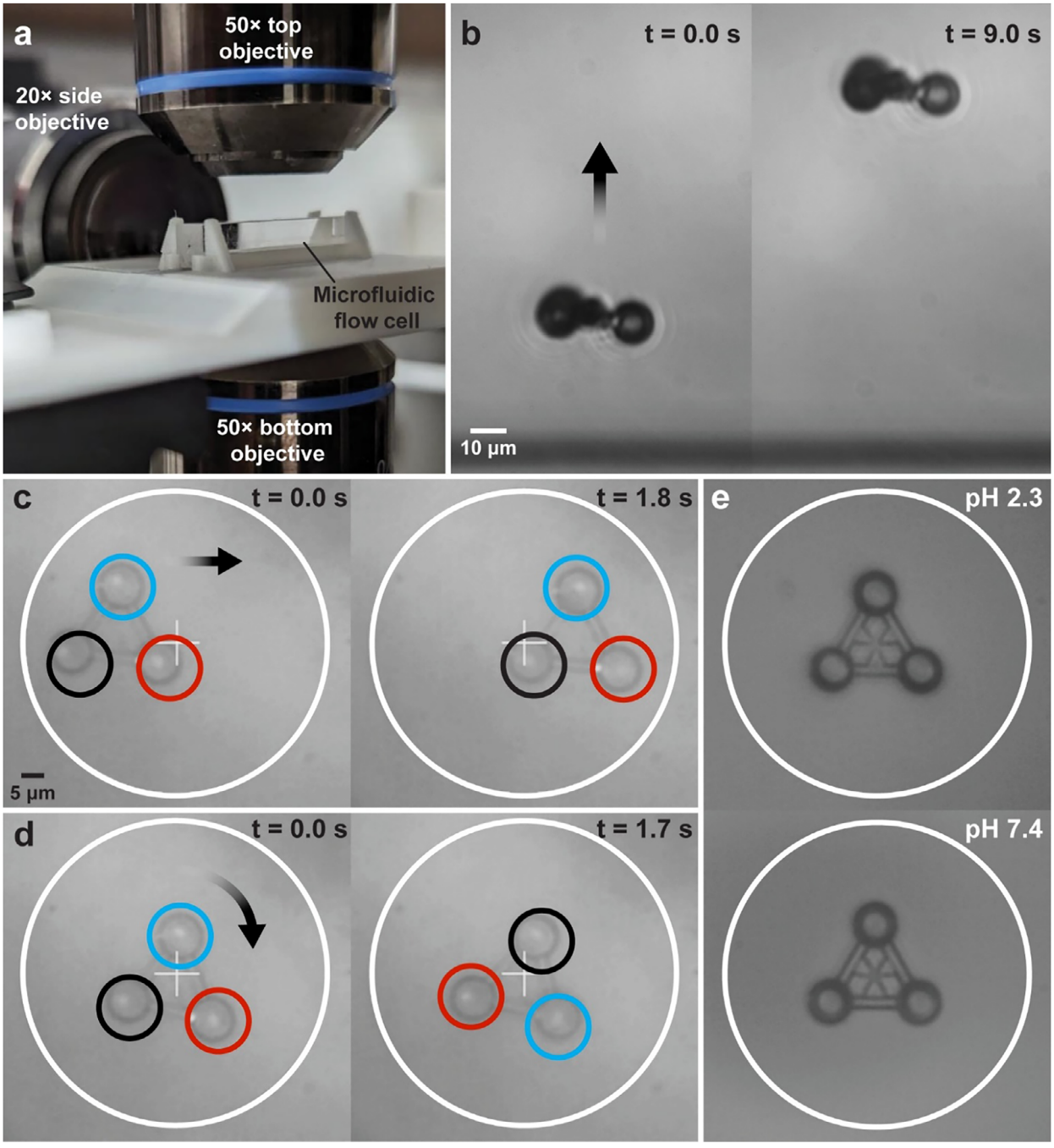

Figure 4. Optical trapping setup and microrobot manipulation. a) Sample stage of the optical trapping setup, showing the microfluidic flow cell placed between the top and bottom objectives. The 20× objective is used to visualize the microrobots from the side. b) Side view snapshots of the microrobot being translated vertically within the flow cell. c) Top-view snapshots of the microrobot being translated in XY within the flow cell. The large white circle represents the trapping area, while the smaller circles represent the optical traps. d) Top view snapshots of the microrobot being rotated in-plane. e) Top view images of the microrobots in pH 2.3 and 7.4 solutions when the bottom objective is unfocused. The three sensing elements touch in the bottom picture, showing that the microrobot is in a neutral environment.

with other techniques, as exemplified in this work by using optical trapping, which enables precise microrobot manipulation.

However, the simplicity of our approach comes with its own limitations in terms of sensing performance, which is only semi-quantitative. The main challenges here are the low signal to noise ratio, and the limited pH range in which our microrobots exhibit a shape change. These should be improved in the future to foster the practical applications of pH sensing microrobots. An important aspect to consider is the material selection for the pH sensing elements. For example, using a material with a higher

shape response could help improve the signal-to-noise ratio by increasing the signal, i.e., shape response. Alternatively, using a material with no volatile components could help improve the signal-to-noise ratio by reducing the noise, i.e., variability. Another aspect to consider is the shape, size, and printing parameters of the sensing elements, which could be further optimized. Finally, to extend the pH range for sensing, the sensing elements could be made using multiple different materials, similar to the use of blue litmus paper for acidic regions and red litmus paper for basic regions.

We envision that our microrobots have potential for different microscale pH sensing applications, where they could be used as custom research tools. For example, the size of the microrobots and the shape response of the sensing elements are suitable for extracellular pH mapping in organ-on-a-chip devices, which as of now is only possible in open cell culture setups or with the use of fluorescent probes.[22] Alternatively, our microrobots could be used to provide visual feedback for pH control in microreactors. The small size and high mobility of the microrobots should also allow for measurements of pH in 3D microfluidic chips. Finally, the small size and the reusability of the microrobots recommend them as a sustainable and cost-effective approach as opposed to, e.g., electrochemical sensors, which are susceptible to fouling over time, or fluorescent probes, which are susceptible to photobleaching.

4. Experimental Section

Materials: Anhydrous acrylic acid (CAS 79-10-7, ID 147230, 99.0%, 200 ppm MEHQ), phenylbis(2,4,6-trimethylbenzoyl)phosphine oxide (CAS 162881-26-7, ID 511447, 97.0%), hydrochloric acid (CAS 7647-01-0, ID 320331, 37.0 wt.%), potassium hydrogen phthalate (CAS 877-24-7, ID P1088, 99.9%), PBS tablets (ID P4417), sodium hydroxide (CAS 1310-73-2, ID 1.60309, 0.01 M), sodium bicarbonate (CAS 144-55-8, ID S6014, 99.7%), 3-(Trimethoxysilyl)propyl methacrylate (CAS 2530-85-0, ID 440159, 98.0%), and sodium dodecyl sulfate (CAS 151-21-3, ID L4509, 98.5%), were purchased from Sigma-Aldrich. Ethoxylated (15) trimethylolpropane triacrylate (CAS 28961-43-5) was purchased from Arkema. Acetic acid (CAS 64-19-7. ID 1.59166, 30 wt.%), was purchased from Merck. Ethanol absolute (CAS 64-17-5, ID 12.03806, 99.8%), and isopropanol (CAS 67-63-0, ID 13.05228, 99.5%), were purchased from VWR. Acetone (CAS 67-64-1, 99.8%) was purchased from Honeywell Research Chemicals. Immersol 518 F (ID 433802-9010-000) was purchased from Zeiss Microscopy. All reagents and solvents were used as received without additional purification.

Round borosilicate glass coverslips (170 µm thick, 30 mm diameter) and IP-L photoresist were purchased from Nanoscribe GmbH. Square glass coverslips (18 mm side length) were purchased from VWR. Borosilicate glass capillary tubes (0.8 mm ID, 1.0 mm OD) were purchased from CM Scientific. Microfluidic flow cells (Type 131.050, 250 × 250 µm square inner cross section, 20 mm length) were purchased from Hellma.

Preparation of pH-Responsive Hydrogel Photoresist: For the pH-responsive hydrogel photoresist preparation, the photoinitiator, which was in powder form, was first weighed inside an amber vial. The monomer and crosslinker, which were both liquid, were then sequentially added inside the vial, using a pipette. The photoresist was protected from both light and moisture during preparation and storage. **Table 1** shows the composition of the photoresist. No solvent was used in the photoresist preparation. To ensure proper mixing, the photoresist was vortexed briefly, sonicated for 5 min, vortexed briefly again, then left to settle overnight at room temperature before being used for printing.

For the swelling experiments, three different photoresist batches were prepared.

Table 1. Composition of the pH-responsive hydrogel photoresist.

Compound	Role	Mol%	Weight%
Phenylbis(2,4,6-trimethylbenzoyl)phosphine oxide	Photoinitiator	0.5	0.7
Acrylic acid	Monomer	50.7	14.7
Ethoxylated (15) trimethylolpropane triacrylate	Crosslinker	48.9	84.6

Preparation of pH Solutions: The pH values of all the solutions were determined using a pH meter (SevenCompact, S220). The solutions were prepared and adjusted to certain pH values as shown in **Table 2**.

Silanization of Substrates: To prevent the microrobots from detaching when performing swelling characterization experiments, the substrates were silanized before printing. Round borosilicate glass coverslips were first rinsed with acetone and isopropanol, then dried with nitrogen. The substrates were then treated with oxygen plasma (Diener Electronic Zepto) for 15 min and placed in a bath with 98.5 vol.% ethanol, 0.5 vol.% acetic acid, and 1.0 vol.% 3-(trimethoxysilyl)propyl methacrylate, where they were kept for 1 h at room temperature. The substrates were then rinsed with isopropanol, dried with nitrogen, and placed on a hotplate at 60 °C for 1 h. After silanization, the substrates were stored in a closed box and used within 1 month.

Microrobot Fabrication: All 3D designs were made using SolidWorks 2023 and exported as. STL files. Three separate. STL files were prepared for the multimaterial microrobot printing. The first. STL file contained the model for the backbone structure, the second contained the model for the hemispheres (used as automated alignment markers), and the third contained the model for the sensing element. The arrows used as rotational alignment markers were prepared in DeScribe by programming the coordinates. Fabrication was done by 2PP micro 3D printing on a Nanoscribe Photonic Professional GT+ (PPGT+) system (Nanoscribe GmbH, Karlsruhe, Germany), which uses 150 fs pulses emitted at 100 MHz by a 780 nm Ti-Sapphire laser. Silanized borosilicate glass coverslips were used as 3D printing substrates in oil immersion configuration using a Plan-APOCHROMAT 63×/1.40 Oil DIC objective (Carl Zeiss, Oberkochen, Germany) objective. All job files used for fabrication are available from: (https://figshare.com/s/cbf7588647f681777d48).

For the first printing step, the. STL files for the backbones and hemispheres were imported into the DeScribe software (version 2.7), where the print parameters were set and the. GWL job file for 3D printing was generated. Most printing parameters follow the standard DeScribe recipe for small features (IP-Dip 63× Fused Silica), with a few modifications described below. Typically, the printing starts 0.5 µm below the identified substrate/photoresist interface, to ensure adhesion of structures to the substrate. To reduce the contact area between the spheres and the glass substrate and thus facilitate detachment of the microrobots for optical

Table 2. Composition and adjustment method of the pH solutions used.

pH value	Composition	pH adjustment
2.3	41.5 µL HCl (37%) + 100 mL DI water.	N/A
4.4	Adjusted from pH 5.2 solution.	0.01 M HCl solution
5.2	45.2 mL NaOH (0.1 M) + 100 mL KHP (0.1 M).	N/A
5.8	Adjusted from pH 5.2 solution.	0.01 M NaOH solution
6.7	Adjusted from pH 7.4 solution.	0.01 M HCl solution
7.4	1 PBS tablet in 200 mL DI water.	N/A
8.8	21.4 mL NaOH (0.1 M) + 100 mL $NaHCO_3$ (0.05 M). Adjusted to desired pH.	0.01 M HCl solution

trapping, an interface value of 0.3 µm was used instead of the default interface value of 0.5 µm. To counteract the beam shift during printing, the *DefocusFactor* command was used, which compensates for shifts in the focal point due to refractive index mismatches between the objective, immersion oil and substrate. A defocus factor of 1.15 was used when printing the IP-L structures and 1.13 when printing the sensing element. The method for determining the defocus factors can be found in the Supporting Information and Figure S3 (Supporting Information). The microrobot backbones were arranged in a 3 × 3 array such that 9 microrobots were printed simultaneously within the effective print field using galvo print mode. The hemispheres were included in a 2 × 2 array intercalated among the backbones. The. GWL file containing the arrows was included in the job file for printing backbones and alignment markers. Multiple backbone arrays, which were separated by 200 µm in the X-direction and 300 µm in the Y-direction, were included in the job file. The stage performs a physical movement using piezo motors in between printing each array. The IP-L photoresist was used as the polymer precursor for the backbone and alignment markers. After this first print step, the backbones and alignment markers were developed in an isopropanol bath for 15 min, followed by immersion in a fresh isopropanol bath for another 15 min, then finally allowed to dry at room temperature.

For the second printing step, the. STL file containing the sensing elements was imported into the DeScribe software, where the print parameters were set and the. GWL job file was generated. To select the print parameters for the sensing element, an initial study was performed by varying the laser power (35–55 mW), scan speed (5–10 mm s^{-1}), slicing distance (0.2–0.4 µm), hatching distance (0.2–0.3 µm), print orientation (0°, 90°, or woodpile), and number of contour lines (0 or 1). From the tested parameters, the following combination was selected as giving the best compromise between the structural integrity and swelling of the structures: 47.5 mW laser power, 5 mm s^{-1} scan speed, 0.3 µm slicing distance, 0.25 µm hatching distance, woodpile print orientation, and no contour lines. These parameters were employed for printing all the multimaterial microrobots used for the sensing experiments presented in this study.

The. STL file contained the sensing elements for a single microrobot, and a 3 × 3 array was generated to match the microrobot backbone array. A print cell was constructed on the top side of the substrate by placing a square glass coverslip supported by two pieces of tape (Figure S4, Supporting Information). The print cell was constructed to minimize evaporation of the acrylic acid present in the hydrogel photoresist. 20 µL of the hydrogel photoresist was dispensed at the side of the cell using a pipette and allowed to gradually fill the cell by capillary effect. The substrate was then reinserted in the PPGT+. Rotational alignment of the print coordinate system was performed manually by acquiring the coordinates of at least two alignment markers (A). The PPGT+ system's software rotates the virtual coordinate system according to the coordinates of the markers. The rotational alignment was only performed once for each substrate, regardless of the number of arrays printed on the substrate. Afterward, the automated alignment program, which aligns the sensing elements to each backbone array, was run (see section "Automated Alignment Program"). After printing the sensing elements, the multimaterial microrobots were developed in an isopropanol bath for 15 min, followed by immersion in a fresh isopropanol bath for another 15 min, then finally allowed to dry at room temperature. The substrates containing the microrobots were stored in a closed box. The fabrication steps and sample storage were done in a cleanroom environment with temperature control between 21.5 and 23.5 °C and humidity control between 45% and 55% relative humidity (RH).

Automated Alignment Program: The automated alignment program was written in the Python programming language using Python version 3.7. The computer vision features were implemented using the OpenCV (Open Computer Vision Library) module (version 4.8.1.78). The ZEN lite (Version 3.0, Zeiss Microscopy) image acquisition software was used for taking screenshots of the microscope view during printing.

After rotational alignment was performed manually as described in section "Microrobot Fabrication", the user starts "ServerMode" by typing in *StartServerMode* on the NanoWrite GWL mini script window and selecting the folder that contains the job file to be printed. The "ServerMode" feature enables the printer to be controlled using a scripting language, i.e., Python. The user then moves the stage so that the first array of backbones was in view. In the program code, the user types in the substrate rotation (obtained during the rotational alignment), the number of rows and columns corresponding to the backbone sets present on the substrate, and runs the program. The automated alignment program autonomously aligns the stage, then prints the job file containing the sensing elements. The program moves across the rectangular array of backbone sets in a meandering path, repeating the automated alignment and printing of the sensing elements until the job file had been printed on the final set of backbones, as defined by the number of rows and columns input by the user.

Microscopy Characterization: Optical microscopy and scanning electron microscopy images were analyzed using ImageJ software (version 1.53).[65]

Microscopy Characterization—Optical Microscopy: Optical microscopy imaging was performed using a VHX-X1F (KEYENCE, Belgium) digital microscope equipped with a VH-ZST dual objective zoom lens (20–2000× magnification) and a VHX-7020 camera. Images were acquired at 2000× magnification and have a pixel size of 0.076 µm $pixel^{-1}$.

Microscopy Characterization—Scanning Electron Microscopy: SEM imaging was performed using a Zeiss Supra 40 VP (ZEISS Microscopy, Oberkochen, Germany) scanning electron microscope. Prior to SEM imaging, the samples were coated with a gold layer of ≈15 nm using a sputter coater (Cressington Scientific Instruments, Watford, UK). All images were acquired in high vacuum mode using an acceleration voltage of 1.5 kV and the secondary electron detector. Samples used for SEM were not used for any subsequent experiments.

Swelling Characterization of Sensing Elements: For each set of swelling experiments, three samples containing nine 4D printed microrobots were prepared, where each sample was printed using a different hydrogel photoresist batch. One set of samples was used for studying the reversibility of the swelling response at two different time points: 1 and 49 days after fabrication. Another set of samples was used for studying the swelling as a function of pH.

The print cell setup used when printing the sensing elements was also used during optical microscopy imaging of the microrobots in different pH solutions (Figure S4, Supporting Information). 10 µL of pH solution were dispensed at the side of the print cell using a pipette. The liquid gradually fills the cell by capillary effect, after which the optical microscopy image was acquired after at least 5 s. The print cell improves the sharpness of the images by keeping the fluid height constant and low. After the image was acquired, a cleanroom tissue was placed at the edge of the cell to absorb the solution. All experiments for characterizing the swelling of the sensing elements were performed in a cleanroom environment with temperature control between 21.5 and 23.5 °C and humidity control between 45% and 55% RH.

For the reversibility test, the nine microrobots on each sample were imaged when immersed in pH 2.3 and 7.4 solutions. After removing the pH solution from the cell and before adding the next pH solution, deionized water was used to rinse the cell. This ensures that no residual solution was left that may affect the swelling of the sensing elements when the next pH solution was added. This process was repeated until the microrobots had been cycled between the two pH values for a total of ten cycles. After the experiments, the samples were stored in air at room temperature. The same experiments were repeated on the same samples after 49 days.

For studying the swelling as a function of pH, the nine microrobots on each sample were imaged when immersed in pH 2.3, 4.4, 5.2, 5.8, 6.7, 7.4, and 8.8 solutions. After removing the pH 8.8 solution from the cell, deionized water was used to rinse the cell before storing the sample in air at room temperature. This process was repeated six times after 1 day, 1 week, 2 weeks, 5 weeks, and 8 weeks of storage.

Three microrobots were selected (one on each row of the 3 × 3 array) on each sample to calculate the percentage increase in the visible area of their sensing elements. All three sensing elements were measured for each of the selected microrobots. The area of the sensing elements when imaged in pH 2.3 was taken as the reference (i.e., 0% area increase). The formula for calculating the percentage increase in area is shown in Equation (1),

where A_{pH} is the area of the sensing element when immersed in a certain pH solution, and $A_{2.3}$ is the area of the sensing element when immersed in the pH 2.3 solution.

$$Area\ Increase\ (\%) = \frac{A_{pH} - A_{2.3}}{A_{2.3}} \times 100\% \quad (1)$$

For the data shown in Figure 3d,e, twenty-seven values were averaged. This corresponds to three sensing elements measured on each of three different microrobots from three different samples prepared using different photoresist batches.

Microrobot Harvesting and Transferring: To detach and transfer microrobots to the microfluidic flow cell for optical trapping, a custom-built microrobot harvesting setup consisting of a microliter syringe (Hamilton, Model 1701 10 µL syringe) mounted on a motorized stage (Thorlabs, Z625B 25 mm DC actuators) (Figure S5, Supporting Information) was used. The motorized stage was positioned next to an inverted microscope (Leica Microsystems, DM IRB) with a camera (ZEISS Microscopy, Axiocam 105 color). A pulled borosilicate glass capillary tube was attached to the syringe. The capillary was prefilled with 0.1 wt.% sodium dodecyl sulfate (SDS) in either a pH 2.3 or pH 7.4 solution. The substrate with printed microrobots was placed on the microscope stage and a drop of the same pH solution with SDS was added on the microrobots. The syringe was moved to selectively detach microrobots. The syringe's plunger was connected to a motor (Thorlabs, Z612B 12 mm DC actuator), which can be controlled precisely and allows for the slow uptake of a detached microrobot into the capillary (Video S3, Supporting Information). Once a microrobot was drawn into the capillary, a microfluidic flow cell was placed on the microscope stage. The flow cell was also prefilled with the same pH solution with SDS. The glass capillary was inserted into the channel using the motorized stage and the plunger motor was actuated to transfer the microrobot into the channel (Video S4, Supporting Information). The flow cell was then placed on the sample stage of the optical trapping setup.

Optical Trapping: Optical trapping was performed in the Biophotonics WorkStation (BWS) that employs counter-propagating beams to control and manipulate microparticles and microstructures (Figure S2, Supporting Information).[55] A counter-propagating beam relies on scattering forces for trapping instead of the gradient force used in more common optical tweezers.[66] In the BWS, the counter-propagating beams were generated using a proprietary illumination module based on generalized phase contrast[54] and a continuous-wave near infrared laser (IPG Photonics, λ = 1070 nm, 40 W maximum input power). The beams were then relayed onto the sample using two opposing objectives (Olympus LMPLN, 50× IR, WD = 6.0 mm NA = 0.55). The top objective relayed the image to a camera (JAI, CV-A10 GE), which was used for recording movement in the XY plane. A 20× microscope objective (Mitutoyo Plan Apo, 20×, WD = 20 mm, NA = 0.42) was used for recording movements in Z using a second camera (ZEISS Microscopy, Axiocam 105 color). A LabView-based graphical user interface was used to generate multiple traps, which were visualized as overlay graphics on the real-time images acquired with the top camera (Figure S6, Supporting Information). Displacement of the microrobot in the XY plane was executed by dragging the trap overlays to the desired location, while manipulation on the Z-axis was performed by changing the intensity ratio of the top and bottom counter-propagating beams. The size of the beam spots can also be adjusted from the graphical user interface. In the experiments, three counter-propagating beams were generated for trapping the microrobots, with one set of counter-propagating beams on each trapping sphere. The trapping beam spot sizes were set to 14 µm. The laser power was set to 40 W at the input. Since the total optical power reaching the sample was in the order of tens of milliwatts due to significant losses in the system, a high input laser power had to be used.

Supporting Information

Supporting Information is available from the Wiley Online Library or from the author.

Acknowledgements

A.-I.B. and D.M. acknowledge funding from Danmarks Frie Forskningsfond (Grant No. 1134-00001B). A.-I.B., M.P. and S.S. acknowledge funding from Novo Nordisk Fonden (Grant No. NNF22OC0079707). Y.T. acknowledges Science Foundation Ireland (Grant No. 18/EPSRC-CDT-3581) and the Engineering and Physical Sciences Research Council (Grant No. EP/S023259/1). L.F. and C.D. acknowledge funding from the European Research Council (Grant No. 802929 – ChemLife and grant number 101077430 – BIO4D). Most of the experimental work was performed inside the PolyFabLab user facility, which was partly funded by Novo Nordisk Fonden (Grant No. NNF21OC0068814).

Conflict of Interest

The authors declare no conflict of interest.

Author Contributions

D.M., A.M.V., and A.-I.B. were responsible for conceptualization. D.M., M.P., S.S., M.F., Y.T., and A.-I.B. developed the methodology. D.M. and S.S. worked on software development. D.M. performed validation and formal analysis. D.M., M.P., S.S., A.M.V., M.F., and Y.T. conducted the investigation. C.D., L.F., and A.-I.B. provided resources. D.M. carried out data curation. D.M. and A.-I.B. wrote the original draft. M.P., S.S., A.M.V., M.F., Y.T., C.D., R.T., L.F., and A.-I.B. reviewed and edited the manuscript. D.M. and A.-I.B. prepared the visualizations. C.D., R.T., L.F., and A.-I.B. supervised the work. A.-I.B. managed the project administration. L.F. and A.-I.B. acquired funding. The manuscript was written through the contributions of all authors. All authors have given approval to the final version of the manuscript.

Data Availability Statement

The data that support the findings of this study are openly available in figshare at https://figshare.com/s/613f35889ab37dbf7bc5, reference number 28389143.

Keywords

4D printing, computer vision, microrobots, optical trapping, sensing, two-photon polymerization

Received: May 21, 2025
Revised: September 2, 2025
Published online: September 27, 2025

[1] S. P. L. Sörensen, *Enzymstudien II: über die Messung und die Bedeutung der Wasserstoffionenkonzentration bei enzymatischen Prozessen*, Springer-Verlag, Berlin, Germany, **1909**, Vol. *21*, pp. 131–304.
[2] J. R. Casey, S. Grinstein, J. Orlowski, *Nat. Rev. Mol. Cell Biol.* **2010**, *11*, 50.
[3] E. W. K. Young, D. J. Beebe, *Chem. Soc. Rev.* **2010**, *39*, 1036.
[4] P. Swietach, R. D. Vaughan-Jones, A. L. Harris, A. Hulikova, *Philos. Trans. R. Soc. B: Biol. Sci.* **2014**, *369*, 20130099.
[5] S. K. Parks, J. Chiche, J. Pouyssegur, *J. Cell. Physiol.* **2011**, *226*, 299.
[6] P. Hossler, S. F. Khattak, Z. J. Li, *Glycobiology* **2009**, *19*, 936.
[7] S. K. Yoon, S. L. Choi, J. Y. Song, G. M. Lee, *Biotechnol. Bioeng.* **2005**, *89*, 345.

[8] J. B. Russell, D. B. Dombrowski, *Appl. Environ. Microbiol.* **1980**, *39*, 604.
[9] E. Yang, L. Fan, J. Yan, Y. Jiang, C. Doucette, S. Fillmore, B. Walker, *AMB Express* **2018**, *8*, 10.
[10] I. Elmahdi, F. Baganz, K. Dixon, T. Harrop, D. Sugden, G. J. Lye, *Biochem. Eng. J.* **2003**, *16*, 299.
[11] S. K. Suh, K. Yuet, D. K. Hwang, K. W. Bong, P. S. Doyle, T. A. Hatton, *J. Am. Chem. Soc.* **2012**, *134*, 7337.
[12] M. Sarsfield, A. Roberts, K. A. Streletzky, P. S. Fodor, C. R. Kothapalli, *Chem. Eng. Technol.* **2021**, *44*, 622.
[13] A. Agha, W. Waheed, I. Stiharu, V. Nerguizian, G. Destgeer, E. Abu-Nada, A. Alazzam, *Discover Nano* **2023**, *18*, 18.
[14] V. Onesto, S. Forciniti, F. Alemanno, K. Narayanankutty, A. Chandra, S. Prasad, A. Azzariti, G. Gigli, A. Barra, A. De Martino, D. De Martino, L. L. del Mercato, *ACS Nano* **2023**, *17*, 3313.
[15] A. Chandra, S. Prasad, H. Iuele, F. Colella, R. Rizzo, E. D'Amone, G. Gigli, L. L. del Mercato, *Chem. – Eur. J.* **2021**, *27*, 13318.
[16] R. Rizzo, V. Onesto, G. Morello, H. Iuele, F. Scalera, S. Forciniti, G. Gigli, A. Polini, F. Gervaso, L. L. del Mercato, *Mater. Today Bio* **2023**, *20*, 100655.
[17] A. Steinegger, O. S. Wolfbeis, S. M. Borisov, *Chem. Rev.* **2020**, *120*, 12357.
[18] D. Harris, J. G. Ummadi, A. R. Thurber, Y. Allau, C. Verba, F. Colwell, M. E. Torres, D. Koley, *Analyst* **2016**, *141*, 2887.
[19] J. S. G. Selva, V. A. Voltarelli, P. C. Brum, M. Bertotti, *Electrochim. Acta* **2023**, *444*, 142015.
[20] Z. Zhu, Z. Ye, Q. Zhang, J. Zhang, F. Cao, *Electrochem. Commun.* **2018**, *88*, 47.
[21] M. C. O. Monteiro, M. T. M. Koper, *Curr. Opin. Electrochem.* **2021**, *25*, 100649.
[22] Y. Zhang, Y. Takahashi, S. P. Hong, F. Liu, J. Bednarska, P. S. Goff, P. Novak, A. Shevchuk, S. Gopal, I. Barozzi, L. Magnani, H. Sakai, Y. Suguru, T. Fujii, A. Erofeev, P. Gorelkin, A. Majouga, D. J. Weiss, C. Edwards, A. P. Ivanov, D. Klenerman, E. V. Sviderskaya, J. B. Edel, Y. Korchev, *Nat. Commun.* **2019**, *10*, 5610.
[23] F. Sun, P. Zhang, T. Bai, D. David Galvan, H.-C. Hung, N. Zhou, S. Jiang, Q. Yu, *Biosens. Bioelectron.* **2015**, *73*, 202.
[24] Y. Liu, S. Yue, Y.-N. Wang, Y. Wang, Z.-R. Xu, *Sens. Actuators, B* **2020**, *310*, 127889.
[25] M. S. A. S. Shawkat, N. McFarlane, 2017 IEEE Sensors, IEEE, UK **2017**.
[26] S. Sinha, T. Pal, D. Kumar, R. Sharma, D. Kharbanda, P. K. Khanna, R. Mukhiya, *Mater. Lett.* **2021**, *304*, 130556.
[27] Y. Wang, M. Yang, C. Wu, *Sensors* **2020**, *20*, 6921.
[28] A.-I. Bunea, D. Martella, S. Nocentini, C. Parmeggiani, R. Taboryski, D. S. Wiersma, *Adv. Intell. Syst.* **2021**, *3*, 2000256.
[29] L. Kong, J. Guan, M. Pumera, *Curr. Opin. Electrochem.* **2018**, *10*, 174.
[30] A.-I. Bunea, I.-A. Pavel, S. David, S. Gáspár, *Biosens. Bioelectron.* **2015**, *67*, 42.
[31] M. N. Popescu, S. Gáspár, *Biosensors* **2023**, *13*, 45.
[32] A.-I. Bunea, R. Taboryski, *Micromachines* **2020**, *11*, 1048.
[33] A.-I. Bunea, N. del Castillo Iniesta, A. Droumpali, A. E. Wetzel, E. Engay, R. Taboryski, *Micro* **2021**, *1*, 164.
[34] F. Cantoni, D. Maher, E. Bosler, S. Kühne, L. Barbe, D. Oberschmidt, C. Marquette, R. Taboryski, M. Tenje, A.-I. Bunea, *Addit. Manuf.* **2023**, *76*, 103761.
[35] S. Hu, R. Hu, X. Dong, T. Wei, S. Chen, D. Sun, *Opt. Express* **2019**, *27*, 16475.
[36] E. Gerena, F. Legendre, A. Molawade, Y. Vitry, S. Regnier, S. Haliyo, *Micromachines* **2019**, *10*, 677.
[37] R. Li, M. Jiang, B. Liu, S. Jiang, C. Chen, M. Liang, L. Qu, C. Wang, G. Zhao, Y. Hu, D. Wu, J. Chu, J. Li, *Lab Chip* **2024**, *24*, 832.
[38] Y. Hou, H. Wang, R. Fu, X. Wang, J. Yu, S. Zhang, Q. Huang, Y. Sun, T. Fukuda, *Lab Chip* **2023**, *23*, 848.
[39] M. Sitti, D. S. Wiersma, *Adv. Mater.* **2020**, *32*, 1906766.
[40] D. Maher, M. Piekarczyk, B. Rezaei, A.-I. Bunea, *Adv. Mater. Technol.* **2025**, *10*, 2401950.
[41] C. Xin, D. Jin, Y. Hu, L. Yang, R. Li, L. Wang, Z. Ren, D. Wang, S. Ji, K. Hu, D. Pan, H. Wu, W. Zhu, Z. Shen, Y. Wang, J. Li, L. Zhang, D. Wu, J. Chu, *ACS Nano* **2021**, *15*, 18048.
[42] Y.-W. Lee, J.-K. Kim, U. Bozuyuk, N. O. Dogan, M. T. A. Khan, A. Shiva, A.-M. Wild, M. Sitti, *Adv. Mater.* **2023**, *35*, 2209812.
[43] U. Bozuyuk, O. Yasa, I. C. Yasa, H. Ceylan, S. Kizilel, M. Sitti, *ACS Nano* **2018**, *12*, 9617.
[44] H. Xu, S. Wu, Y. Liu, X. Wang, A. K. Efremov, L. Wang, J. S. McCaskill, M. Medina-Sánchez, O. G. Schmidt, *Nat. Nanotechnol.* **2024**, *19*, 494.
[45] Z.-C. Ma, Y.-L. Zhang, B. Han, X.-Y. Hu, C.-H. Li, Q.-D. Chen, H.-B. Sun, *Nat. Commun.* **2020**, *11*, 4536.
[46] S. Ji, X. Li, Q. Chen, P. Lv, H. Duan, *Adv. Intell. Syst.* **2021**, *3*, 2000270.
[47] F. Rajabasadi, S. Moreno, K. Fichna, A. Aziz, D. Appelhans, O. G. Schmidt, M. Medina-Sánchez, *Adv. Mater.* **2022**, *34*, 2204257.
[48] P. Zhou, Z. Zhang, F. Mo, Y. Wang, *Adv. Sensor Res.* **2024**, *3*, 2300021.
[49] R.-I. Stoian, B. K. Lavine, A. T. Rosenberger, *Talanta* **2019**, *194*, 585.
[50] A. V. Saetchnikov, A. E. Tcherniavskaia, V. A. Saetchnikov, A. Ostendorf, *Light: Adv. Manuf.* **2024**, *5*, 624.
[51] Z. Yu, L. Li, F. Mou, S. Yu, D. Zhang, M. Yang, Q. Zhao, H. Ma, W. Luo, T. Li, J. Guan, *InfoMat* **2023**, *5*, 12464.
[52] K. Liu, H. Ding, Z. Chong, Y. Zeng, Y. Niu, J. Zhang, Y. Kang, X. Du, Z. Gu, *Chem. Eng. J.* **2024**, *482*, 148679.
[53] S. Zhang, F. Mou, Z. Yu, L. Li, M. Yang, D. Zhang, H. Ma, W. Luo, T. Li, J. Guan, *Nano Lett.* **2024**, *24*, 5958.
[54] A.-I. Bunea, J. Glückstad, *Laser Photonics Rev.* **2019**, *13*, 1800227.
[55] E. Engay, A.-I. Bunea, M. Chouliara, A. Bañas, J. Glückstad, *Opt. Lett.* **2018**, *43*, 3870.
[56] M. Schmid, D. Ludescher, H. Giessen, *Opt. Mater. Express* **2019**, *9*, 4564.
[57] L. J. Jiang, Y. S. Zhou, W. Xiong, Y. Gao, X. Huang, L. Jiang, T. Baldacchini, J.-F. Silvain, Y. F. Lu, *Opt. Lett.* **2014**, *39*, 3034.
[58] T. Baldacchini, V. Nunez, C. N. LaFratta, J. S. Grech, V. I. Vullev, R. Zadoyan, *Laser 3D Manuf. II* **2015**, *9353*, 104.
[59] J. Zheng, H. Yu, Y. Zhang, J. Wang, H. Guo, H. Luo, X. Wang, Y. Qiu, L. Liu, W. J. Li, *Small* **2024**, *20*, 2311951.
[60] H. N. Po, N. M. Senozan, *J. Chem. Educ.* **2001**, *78*, 1499.
[61] M. R. Bayat, M. Baghani, *J. Intell. Mater. Syst. Struct.* **2021**, *32*, 2349.
[62] A. Richter, G. Paschew, S. Klatt, J. Lienig, K.-F. Arndt, H.-J. P. Adler, *Sensors* **2008**, *8*, 561.
[63] U. Hwang, H. Moon, J. Park, H. W. Jung, *Polymers* **2024**, *16*, 2149.
[64] S. Hocine, D. Ghemati, D. Aliouche, *Polym. Bull.* **2023**, *80*, 12591.
[65] C. A. Schneider, W. S. Rasband, K. W. Eliceiri, *Nat. Methods* **2012**, *9*, 671.
[66] A. Ashkin, J. M. Dziedzic, J. E. Bjorkholm, S. Chu, *Opt. Lett.* **1986**, *11*, 288.